Photoinduced charge transfer renormalization in NiO

Tobias Lojewski,[1] Denis Golež [ID],[2,3] Katharina Ollefs [ID],[1] Loïc Le Guyader [ID],[4] Lea Kämmerer,[1] Nico Rothenbach,[1]
Robin Y. Engel [ID],[5] Piter S. Miedema [ID],[5] Martin Beye [ID],[5,6] Gheorghe S. Chiuzbăian [ID],[7] Robert Carley,[4] Rafael Gort,[4]
Benjamin E. Van Kuiken,[4] Giuseppe Mercurio [ID],[4] Justina Schlappa,[4] Alexander Yaroslavtsev,[4,8,9] Andreas Scherz [ID],[4]
Florian Döring,[10] Christian David,[10] Heiko Wende [ID],[1] Uwe Bovensiepen [ID],[1,11] Martin Eckstein,[12]
Philipp Werner [ID],[13] and Andrea Eschenlohr [ID][1,*]

[1]*Faculty of Physics and Center for Nanointegration Duisburg-Essen (CENIDE), University of Duisburg-Essen,
Lotharstr. 1, 47057 Duisburg, Germany*
[2]*Jozef Stefan Institute, Jamova 39, 1000 Ljubljana, Slovenia*
[3]*Faculty of Mathematics and Physics, University of Ljubljana, Jadranska 19, 1000 Ljubljana, Slovenia*
[4]*European XFEL, Holzkoppel 4, 22869 Schenefeld, Germany*
[5]*Deutsches Elektronen-Synchrotron DESY, Notkestr. 85, 22607 Hamburg, Germany*
[6]*Department of Physics, AlbaNova University Center, Stockholm University, SE-10691 Stockholm, Sweden*
[7]*Sorbonne Université, CNRS, Laboratoire de Chimie Physique - Matière et Rayonnement, 75005 Paris, France*
[8]*Department of Physics and Astronomy, Uppsala University, 75120 Uppsala, Sweden*
[9]*MAX IV Laboratory, Lund University, Box 118, 221 00 Lund, Sweden*
[10]*Paul Scherrer Institut, Forschungsstr. 111, 5232 Villigen PSI, Switzerland*
[11]*Institute for Solid State Physics, The University of Tokyo, Kashiwa, Chiba 277-8581, Japan*
[12]*I. Institute of Theoretical Physics, University of Hamburg, 20355 Hamburg, Germany*
[13]*Department of Physics, University of Fribourg, 1700 Fribourg, Switzerland*

Photodoped states in strongly correlated charge-transfer insulators are characterized by d-d and d-p interactions and the resulting intertwined dynamics of charge excitations and local multiplets. Here, we use femtosecond x-ray absorption spectroscopy in combination with dynamical mean-field theory to disentangle these contributions in NiO. Upon resonant optical excitation across the charge-transfer gap, the Ni L_3 and O K absorption edges red-shift for >10 ps, which we associate with photoinduced changes in the screening environment. An additional signature below the Ni L_3 edge is identified for <1 ps, reflecting a transient nonthermal population of local many-body multiplets. We employ a nonthermal generalization of the multiplet ligand field theory and argue that this feature originates from d-d transitions. Overall, the photodoped state differs significantly from a chemically doped state. Our results demonstrate that x-ray spectroscopies are helpful in revealing excitation pathways in correlated materials.

I. INTRODUCTION

Strongly correlated materials host some of the most intriguing states of matter because of the competition between interaction-induced localization and the itinerant nature of electrons, and they are therefore ideal candidates to realize material control on ultrafast timescales [1–3]. Paradigmatic examples are Mott and charge-transfer (CT) insulators, whose optical properties are determined by the charge transfer between the ligand (typically p) and the correlated orbital (typically d) states [4–6]. Element- and site-selective information on many-body states in such materials can be obtained by resonant soft x-ray absorption and emission spectroscopies [7–9], complementing optical spectroscopy [10,11]. A comparison of core level absorption edges and their fine structure with cluster calculations [12–17] or dynamical mean-field theory (DMFT) [18–20] can provide detailed information about the CT gap, Coulomb repulsion [12,21–23], d-d multiplet excitations [8,24], and the hybridization between the ligand and correlated orbitals [25,26]. Furthermore, ligand absorption edges probe the itinerant states [25], whose nature is crucial for understanding the low-energy physics in chemically doped systems [27–29].

Femtosecond time-resolved x-ray spectroscopy is sensitive to low-energy excitations and transient energy shifts [30–35]. It is, thus, a potentially powerful tool for investigating photoexcited nonequilibrium states in Mott and CT insulators. Recently, a strong subgap excitation has been shown to modify the gap size during the pulse both in cuprate [36] and nickelate [37,38] CT insulators. These effects can be attributed to photo-manipulations of the screening environment [36], the magnetic order [37], or the hybridization between correlated and itinerant orbitals [38], coined dynamical Franz-Keldysh effect [39]. A natural open question is how this picture changes in the case of resonant excitations, which

create long-lived charge carriers in the conduction band, and lead to so-called photodoped states, which may host various nontrivial quantum phases [40–43]. To understand these states, and to potentially design targeted excitation pathways, it is important to clarify the different nature of the charge carriers in photodoped and chemically doped states, and to disentangle effects such as band shifts owing to dynamical screening [44,45] and charge redistribution between orbitals [44,46–48] from the dynamics of Mott excitons or electronic d-d excitations [49–52].

In this paper, we demonstrate for the paradigmatic CT insulator NiO how time-resolved x-ray absorption spectroscopy (tr-XAS) combined with nonequilibrium dynamical mean-field theory (DMFT) [53,54] can provide this type of information for resonantly pumped systems. We identify energy shifts and lineshape modifications in the excitonic peaks at the Ni L_3 and O K absorption edges, and link them to orbital occupations and the screening environment. In addition, we resolve a short-lived Ni L_3 pre-edge feature that represents many-body multiplets, i.e., d-d excitations, as confirmed by the nonthermal generalization of multiplet ligand field theory.

The rest of this paper is organized as follows. In Sec. II A we present the tr-XAS data for photoexcited NiO. Section II B analyzes these results by considering a simple cluster model, GW+DMFT simulations of a charge-transfer insulator model, and nonthermal multiplet ligand field theory. The conclusions are presented in Sec. III. Details of the experimental and computational methods as well as additional DMFT results for a two-orbital Hubbard model are provided in the Appendices.

II. RESULTS

A. Experimental findings

Figure 1(a) shows a sketch of tr-XAS at the Ni L_3 ($2p_{3/2} \rightarrow 3d$) and O K ($1s \rightarrow 2p$) edges. The experiments were performed at room temperature at the Spectroscopy and Coherent Scattering (SCS) instrument of European XFEL using a pump-probe setup with an effective time resolution of 80 fs [35,55]. The data [56] is acquired in transmission geometry using the transmission zone plate and grating setup [55,57] and DSSC detector [58], with a monochromatized x-ray beam with approximately 350 meV energy resolution. Laser pulses with 4.7 eV photon energy, 35 fs pulse duration, and 0.8 mJ/cm^2 or 4 mJ/cm^2 incident fluence were employed to pump 37-nm-thick polycrystalline NiO films above the CT gap (for more information on the sample characterization and experimental details see Appendices A and B). This pumping involves excitations from the O $2p$ states to the upper Hubbard band (UHB) [51], see Fig. 1(a). Figure 1(b) depicts the O K and Ni L_3 XAS signals before and after photoexcitation at a pump-probe delay of $\Delta t = 0.5$ ps, with the pump-induced difference ΔXAS shown by the gray dots. We find a spectral shift of all features, labeled as (1)–(6), to lower x-ray photon energies, as indicated by the derivative-like shape of ΔXAS. We also measured the time dependence at fixed photon energies at both edges, see Fig. 2(a). Exponential fits to these transients, convoluted with 80 fs time resolution [35], indicate a rise time of 99 ± 20 fs for 4.0 mJ/cm^2 pump fluence at the Ni L_3 edge and 580 ± 140 fs
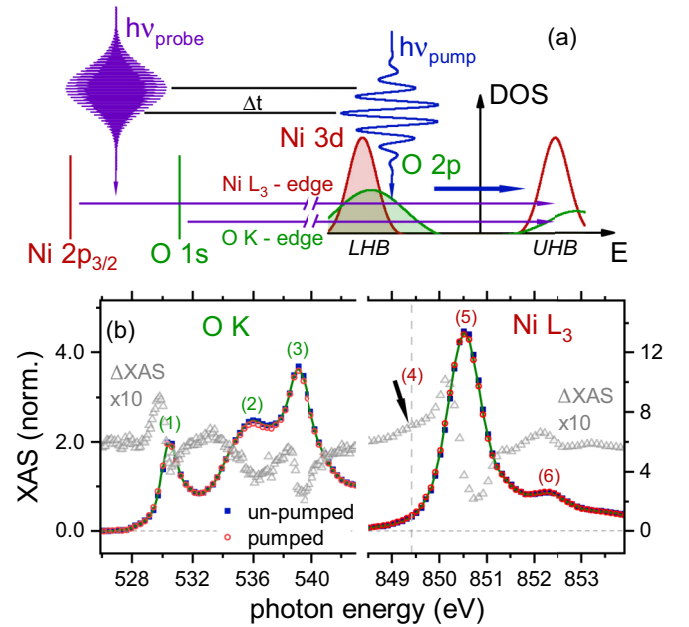
FIG. 1. (a) Transitions by the optical pump $h\nu_{\text{pump}}$ and the x-ray probe $h\nu_{\text{probe}}$, which is delayed by Δt. (b) Ground-state (blue squares) and pumped (red circles) XAS at the O K (left) and Ni L_3 edges (right) for $\Delta t = 0.5$ ps and 4 mJ/cm^2 fluence. The pumped XAS are modeled based on the static XAS (green line), see Appendix B. The gray data show the pump-induced difference ΔXAS vertically offset.

at the O K edge. These energy shifts build up, reach a plateau within 2 ps, and decay on longer timescales. This is in contrast to previous tr-XAS on NiO upon subgap pumping, which showed (smaller) modifications only during the pulse [37,38]. We attribute the difference to the presence of long-lived holon-doublon pairs after the above-gap excitation. These cannot recombine because of the kinetic constraints [3,59,60] and modify the screening environment [61,62].

In the first analysis, we compare the spectra of the photoexcited system to curves modelled by a red-shift ΔE and a broadening $\Delta \Gamma$ of the static spectra, cf. Fig. 2(b). In Fig. 2(c) we plot the best fit ΔE and $\Delta \Gamma$ at $\Delta t = 0.5$ ps as a function of the excitation density dn, i.e., the density of pump-excited electrons relative to all valence electrons (see Appendix B for the determination of dn). The changes in the broadening (or, since $\Gamma \propto 1/\tau$, the changes in the lifetime) are larger for the itinerant p than for the d electrons [35]. Such transient spectral broadening was previously shown to result from lattice excitation [32,63].

We find both the spectral red-shift and broadening to be long-lived. Coherent lattice excitations, like the trapping of photodoped charge carriers by polaron formation [64,65], have been shown to cause extremely long-lived states [66] and were previously found on few ps timescales in NiO [67]. The formation of polarons in NiO is predicted to occur by trapping a photoexcited electron on a Ni site through an expansion of the surrounding oxygen lattice [68], which would be expected to result in a spectral broadening of the O K edge, as is indeed observed by us, see Fig. 2. We thus expect that charge carrier trapping through polaron formation contributes to the long
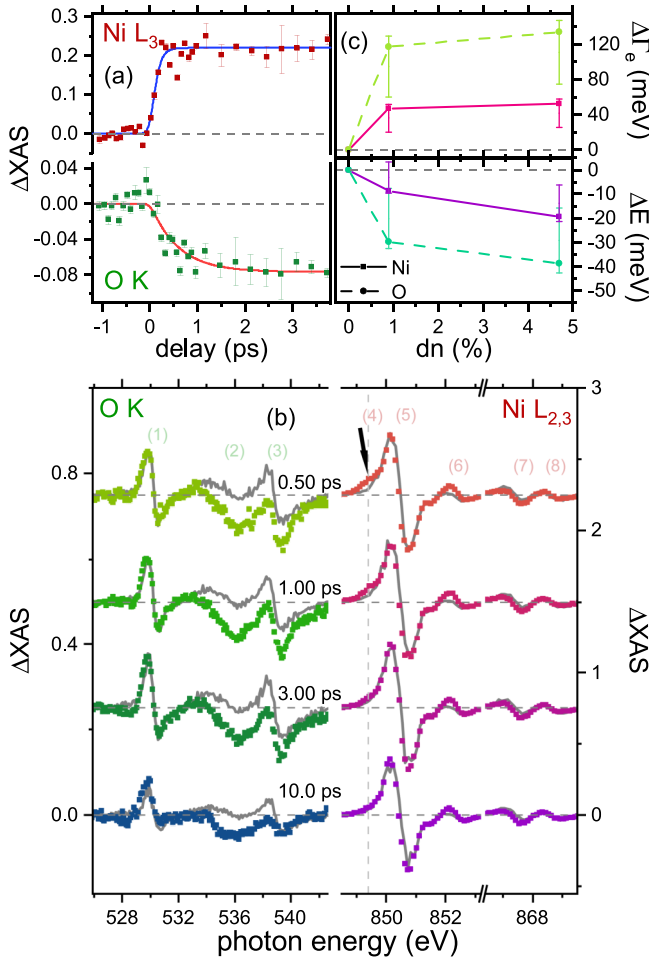
FIG. 2. (a) Time-dependence of ΔXAS for photon energy 539.15 eV (O K) and 850.15 eV (Ni L_3), with exponential fits (lines), for the excited charge carrier density $dn = 4.7\%$ (see Appendix B for the determination). (b) ΔXAS at the O K and Ni L_3 edges for 4 mJ/cm^2 fluence at the indicated Δt and offset vertically. The gray lines show results obtained by a shift ΔE and broadening $\Delta \Gamma$ of the static spectra, see Appendix B. The best fit is used to determine these two parameters. (c) ΔE and $\Delta \Gamma$ at the O K and Ni L_3 edges from fits in (b) as a function of dn determined at $\Delta t = 0.5$ ps.

lifetime of the photoexcited state (for additional information on these long-lived excitations see Appendix C).

While some parts of the spectrum can be reproduced by the shift and broadening, there are important differences: These include parts of the O K spectrum around 536 eV, as well as an additional pump-induced feature in the pre-edge region of the Ni L_3 edge [see vertical arrow in Fig. 2(b)], which decays within less than 3 ps.

B. Theoretical analysis

In the first part of the theoretical analysis, we discuss the microscopic origin of the bandgap renormalization from the point of view of changes in the screening environment. We also comment on lattice and heating effects. In the second part, we analyze the photoinduced pre-edge feature using nonthermal multiplet ligand field theory.

1. Simple cluster model

We here focus on the electronic contribution to the bandgap renormalization. The red-shift is a generic consequence of photodoping in CT insulators, which arises simultaneously from (i) dynamical screening of the Coulomb interaction parameters on the transition metal site, and (ii) nonlocal Coulomb interactions between photodoped ligand holes and electrons in the core and valence orbitals (Hartree shift) [39,44,45]. As a first illustration, consider a simple cluster consisting of a valence (d), core (c), and ligand (p) orbital, with density-density Coulomb interactions U_{dd}, U_{cd}, U_{pd}, U_{cp}, but no p-d hybridization. Upon photoexcitation, the XAS energy for the transition from the core level to the valence d level will shift like $\Delta E_{XAS} = [\Delta U_{dd} + \Delta \epsilon_d - \Delta \epsilon_c - \Delta U_{cd}] + [\Delta N_p (U_{pd} - U_{cp})]$. Here, the first square bracket represents the change of the local interactions (U_{dd}, U_{cd}) and level positions (ϵ_d, ϵ_c) by modified screening [44,45], while the second term is a Hartree shift due to the addition of ligand holes ($\Delta N_p = N_p - N_p^{(0)}$ is the change in the total ligand occupation).

2. GW+DMFT

To demonstrate that such Coulomb shifts prevail beyond the simple model considered in the previous subsection, we perform a lattice simulation, which includes both a microscopic description of dynamical screening and Hartree shifts. We employ a minimal model for a CT insulator, the Emery model [69], which contains one transition metal d orbital and two oxygen p orbitals per unit cell. For numerical reasons, we restrict the modeling to a two-dimensional lattice and the paramagnetic phase. The p_x and p_y orbitals are located on the x and y bonds between the d sites, respectively. We do not expect that two- and three-dimensional models show qualitative differences, since the dominant effects are mainly local. The introduction of antiferromagnetic correlations should enhance the gap reduction after the photoexcitation and contribute to a larger renormalization of the main excitonic resonance [37].

The Hamiltonian of the Emery model is given by

$$H_{dp} = H_e + H_{kin} + H_{int},$$

$$H_e = \epsilon_d \sum_i n_{id} + \epsilon_p \sum_i \left(n_{ip_x} + n_{ip_y} \right),$$

$$H_{kin} = \sum_{\langle i,j \rangle, \sigma, (\alpha, \beta)} (t_{ij}^{\alpha\beta} + \vec{E} \cdot \vec{D}_{ij}^{\alpha\beta}) e^{-\iota \varphi_{ij}} c_{i\alpha\sigma}^\dagger c_{j\beta\sigma},$$

$$H_{int} = U_{dd} \sum_i n_{id\uparrow} n_{id\downarrow} + U_{pd} \sum_i n_{id} N_{i,p}, \quad (1)$$

where $c_{i\alpha\sigma}$ is the annihilation operator for unit cell i and orbital $\alpha \in \{d, p_x, p_y\}$ with spin σ, and $n_{i,\alpha,\sigma}$ is the corresponding density operator, and $n_{i,\alpha} = \sum_\sigma n_{i,\alpha,\alpha}$. In the interaction term H_{int}, $N_{i,p}$ measures the total occupation on the four p orbitals, which connect to the d site in unit cell i (in total two p_x and two p_y orbitals). The energy splitting $\Delta = \epsilon_p - \epsilon_d$ is chosen such that the oxygen orbitals in the atomic limit are completely filled. The hopping matrix $t_{ij}^{\alpha\beta}$ takes a nonzero value t^{dp} for hopping between nearest neighbor d and p_x, p_y orbitals, and t^{pp} for hopping between the p_x and p_y orbitals; $-t_{ii}^{\alpha\alpha} = \mu$ is the chemical potential. We excite the

system by an electric field pulse, described by a homogeneous vector potential $\vec{A}(t)$ and an electric field $\vec{E}(t) = -\partial_t \vec{A}(t)$. The vector potential enters into the kinetic part of the Hamiltonian via the Peierls phase $\varphi_{ij} = e/\hbar \int_{R_i}^{R_j} d\vec{r} \vec{A}(t)$, while the electric field couples via a dipolar matrix element $\vec{D}_{ij}^{\alpha\beta}$ to the interorbital transitions [70]. The specific shape of the electric field used is $E(t) = E_0 \exp^{-4.6(t-t_0)^2/t_0^2} \sin(\omega(t - t_0))$, where E_0 is the amplitude of the field and t_0 is chosen such that the pulse includes four oscillations.

We adjust the interaction and hopping parameters by comparing the equilibrium spectral function with LDA+DMFT results for NiO [28], leading to $U_{dd} = 7.5$ eV, $t^{dp} = 0.37$ eV, $t^{dd} = -0.3$ eV, $U_{pd} = 1.0$ eV, and $\Delta = -4.0$ eV. The dipolar matrix element was chosen as $D = 0.3 e_0 a$, where a is the lattice distance and e_0 is the electron charge. We solve the dynamics after the photoexcitation in the valence space using a nonequilibrium implementation of the GW+EDMFT method, which treats strong correlation and screening effects on the same footing, see Refs. [44,70] for details. In the simulations, we adjust the amplitude of the electric field E_0 such that the pulse produces a certain photoexcitation density dn. The latter is measured as a change of the density of the d orbital $dn = n_d(t_{\text{fin}}) - n_d(t = 0)$, where t_{fin} is the final propagation time.

The XAS signal is calculated by solving an auxiliary impurity problem that includes an additional core-level with a lifetime $1/\Gamma$ ($\Gamma = 0.05$ fs^{-1}); see Ref. [71,72] and Appendix D for details. X-ray energies are measured relative to the position of the main excitonic resonance $|E_c|$ in the equilibrium spectrum.

In the simulation, the photoexcited charge carriers quickly relax to the edge of the charge-transfer gap and are then trapped due to kinetic constraints. While the full GW+DMFT simulations are restricted to short times, previous DMFT simulations for a comparable gap demonstrated a long (ps) lifetime of the photodoped charge carriers [73]. We therefore expect that also the XAS signal will not change much on this scale, and can be compared to the long-lived experimental signal in the photodoped state. The results in Fig. 3 confirm an almost rigid red-shift of the XAS line after photodoping. The relative importance of the Hartree shift and dynamical screening does not affect this qualitative behavior, but only the magnitude of the shift [compare in Fig. 3(c) the results for $U_{cp} = U_{pd} = 1$ eV, for which the Hartree shifts in the atomic model cancel, and those for $U_{cp} = 0$]. This indicates that the Coulomb shift of the XAS exciton is a generic feature of photodoped systems, which arises jointly from the dynamical screening of the local interactions and Hartree shifts.

The analyzed state is highly nonthermal, and on the accessible timescales, it is hard to separate photodoping and hot electron contributions to the modified screening. We performed a set of thermal high-temperature calculations and confirmed that the XAS resonance shift is small as long as the electron temperature is smaller than the gap size. The latter corresponds to roughly 40 000 K, which is much higher than the expected heating effects in the experiments. Polaronic effects (stretching of the Ni-O distance) [65] are further candidates for the bandgap renormalization [74,75] and future improvements in the time resolution should enable a separa-
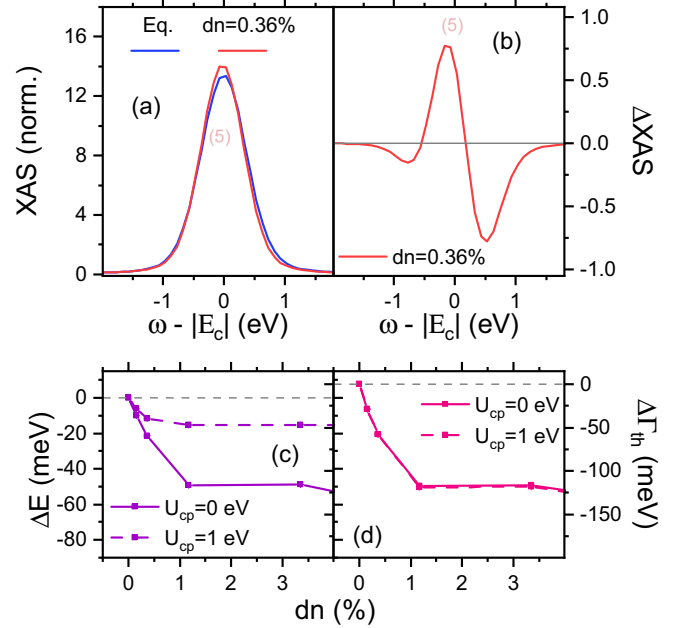
FIG. 3. (a) Calculated equilibrium XAS (blue) and photodoped XAS (red line) at photodoping $dn = 0.36\%$ and a delay of $\Delta t = 7$ fs after the pulse, with the photoinduced change ΔXAS in (b). Shift ΔE (c) and lifetime change $\Delta\Gamma$ (d) of the exciton peak versus photodoping dn determined from the calculations for the given values of the core-oxygen interaction U_{cp} and $U_{dd} = U_{cd} = 7.5$ eV.

tion of the electronic and lattice contributions owing to their different timescales.

Our calculations show that the red-shift increases linearly with the photodoping density and then saturates [Fig. 3(c)], which is in agreement with the experiment [Fig. 2(c)]. A notable difference to the experiment is that the spectra in the simulations do not broaden but become even more narrow [cf. Figs. 1(a) and 3(a)]. This may be because the simulation does not capture additional scattering channels, which can lead to a change of the lineshape of the exciton, such as lattice (polaron) [65] fluctuations.

An interesting question is whether time-resolved XAS can disentangle the different contributions to the Coulomb shift. Assuming a cancellation of the Hartree shifts ($U_{cp} = U_{pd}$) and no screening of U_{cd}, ΔXAS would measure the change of the Hubbard interaction ΔU_{dd}, as concluded previously [36]. However, the observed energy shifts [see Fig. 2(c)] of less than 100 meV are small compared to the interaction parameters, so that a statement on the detailed origin of the shift would require precise knowledge of U_{dd}, U_{cd}, U_{pd}, and U_{cp}, which is beyond the capability of current first principles approaches such as constrained RPA [76]. These difficulties prevent a clear quantification of the relative importance of Hartree shifts and dynamical screening and we expect that both contributions are significant. Nevertheless, our analysis proves a high sensitivity of ΔXAS to the microscopic interactions and therefore shows that time-resolved XAS can give information on various Coulomb parameters (and their changes upon photodoping) that is not easily obtained otherwise, including the nonlocal terms U_{pd} and U_{cp}, which are often neglected even in equilibrium [7,21].
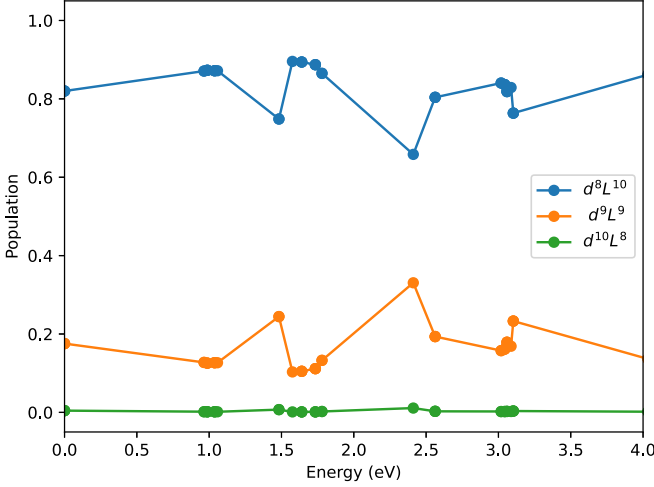
FIG. 4. Weights of the different charge configurations, namely d^8L^{10}, d^9L^9, and $d^{10}L^8$ for the lowest-lying eigenstates. The dots mark the actual data, while the lines are a guide to the eye.

3. Nonthermal multiplet ligand field theory

We now turn to the microscopic origin of the photoinduced pre-edge feature. In this section, we discuss a cluster model that captures the full d-shell's multiplet structure in NiO. In Appendix E, we consider a simplified description with two active e_g orbitals and show that it is possible to understand how local many-body multiplets manifest themselves in the time-resolved XAS signal after a photoexcitation by studying the two-orbital Hubbard model (in the atomic limit and using DMFT).

A particularly interesting finding is the transient pre-edge feature in the Ni L_3 ΔXAS at $\Delta t = 0.25$ ps [Fig. 5(a) below], which is absent at the longest delay times [see Fig. 2(b)]. This motivates an analysis of the multiplet structure of NiO beyond our simple charge-transfer insulator model. Reference [71] showed that the positions of the excitonic resonances in the XAS signal of photoexcited systems within time-dependent DMFT can be well reproduced by atomic limit calculations and that their relative amplitudes in the full many-body state on the lattice allow to measure the time-dependent weight of
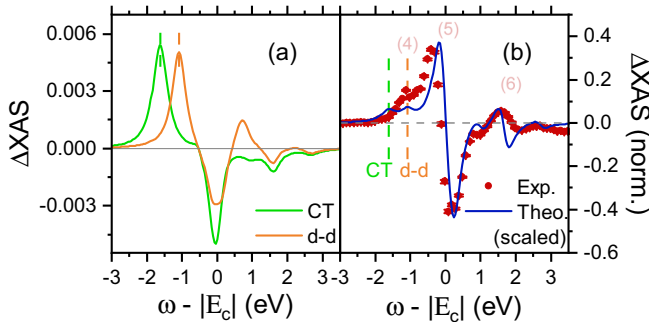
FIG. 5. (a) Change ΔXAS$[\omega, \alpha_a]$ in the XAS signal due to the nonthermal population of a low-lying excited state of predominantly d-d excitation character ($\alpha_3 = 0.02$) or charge-transfer (CT) character ($\alpha_{12} = 0.02$). (b) Comparison of ΔXAS between experiment (Ni L_3, $\Delta t = 0.25$ ps) and theory for nonthermal orbital populations, with the blue curve scaled to match experiment at transient feature (5). The thermal reference spectrum was calculated for $T = 100$ K.

the different local multiplets. This observation motivates us to generalize the multiplet ligand theory [16] to nonthermal distributions [77]. Such an analysis allows us to distinguish between photoinduced d-d transitions and charge-transfer excitations, in contrast to earlier cluster studies [12,13].

We follow the standard procedure and define an extended Anderson impurity problem, starting from the DFT electronic structure [18,26]. This impurity problem is then solved by standard exact-diagonalization techniques (Krylov-based solver), as implemented in EDRIXS [78]. We consider one bath orbital. As we have access to the eigenfunctions $|i\rangle$ of the system, we can directly evaluate the XAS signal as

$$I_{\mathrm{XAS}}(\omega_{\mathrm{in},\epsilon}) = \sum_{i,n} \rho_{ii} |\langle n|\vec{P}_i|i\rangle|^2 \frac{\Gamma_c/\pi}{(\omega_{\mathrm{in}} - (E_n - E_i))^2 + \Gamma_c^2},$$
$$(2)$$

where E_i is the ith eigenenergy and we have introduced the diagonal elements of the density matrix $\rho_{ii} = \frac{1}{Z}e^{-\beta E_i}$. The broadening of the excitonic resonance is determined by the decay time of the core hole. We use the broadening parameter $\Gamma_c = 0.24$ eV. ω_{in} is the energy of the incident x-rays, which is tuned to a specific resonant edge. The transition operator for the dipole transitions is given by $\vec{P}_i = \sum_{i,j} \vec{\epsilon} \sum_R e^{i\vec{k}_i\vec{R}} \vec{r}$, where $\vec{\epsilon}$ is the polarization vector of the incident pulse and $\vec{r}$ is the position operator of electrons measured from the center $\vec{R}$. We evaluate the signal for isotropic polarization, which corresponds to an experiment on a powder sample.

To represent the photoexcited state, we employ the nonthermal occupations

$$\rho_{ii}[\alpha_a] = \frac{\rho_{ii}^{\mathrm{th}} + \alpha_a \delta_{ia}}{\mathrm{Tr}\left[\rho_{ii}^{\mathrm{th}} + \alpha_a \delta_{ia}\right]} \qquad (3)$$

in Eq. (2), with α_a parametrizing the extra weight for the ath eigenstate relative to the thermal values. The rationale behind this ansatz is that the high-energy excitations will quickly relax to the edge of the upper and lower Hubbard band but then encounter a bottleneck in the further relaxation due to the large Mott gap [3,59,60]. This means that the metastable state will primarily exhibit signatures of the low-lying excited states. Therefore, it is instructive to understand the properties of the low-lying states within the multiplet ligand field theory. For a detailed discussion of the method, we refer to Appendix F.

In Fig. 4, we plot the weights of the lowest-lying eigenstates corresponding to two holes on the d orbital d^8L^{10}, a charge-transfer excitation d^9L^9 and a double charge-transfer excitation $d^{10}L^8$. We present the same information for the first 15 eigenstates in Table I. First, the ground state is spin $S = 1$ and is threefold degenerate. Above the ground state, eight states are very close in energy (from 0.96 eV to 1.06 eV). Their orbital character shows that the occupation of the d^8L^{10} state is slightly higher than in the ground state, meaning that these correspond to d-d excitations. Finally, charge-transfer excitations take place at energy $\omega = 1.48$, which we will mark with CT in Fig. 5.

With this information, we can now discuss the photoinduced difference between the nonthermal state and the ground state, ΔXAS$[\omega, \alpha_a] = $ XAS$(\omega, \rho[\alpha_a])$-XAS$(\omega, \rho^{\mathrm{th}})$,

TABLE I. List of the lowest lying eigenvalues with their excitation energies $E - E_0$ and weights of the different orbital configurations d^8L^{10}, d^9L^9, and $d^{10}L^8$. Same data as in Fig. 4.

N	$E-E_0$ [eV]	d^8L^{10}	d^9L^9	$d^{10}L^8$
0	0.0	0.82	0.18	0.0
1	0.0	0.82	0.18	0.0
2	0.0	0.82	0.18	0.0
3	0.96	0.87	0.13	0.0
4	0.96	0.87	0.13	0.0
5	0.99	0.87	0.13	0.0
6	0.99	0.87	0.13	0.0
7	0.99	0.87	0.13	0.0
8	1.04	0.87	0.13	0.0
9	1.04	0.87	0.13	0.0
10	1.04	0.87	0.13	0.0
11	1.06	0.87	0.13	0.0
12	1.48	0.75	0.24	0.01
13	1.48	0.75	0.24	0.01
14	1.58	0.9	0.1	0.0
15	1.64	0.89	0.1	0.0

see Fig. 5(a). As mentioned above, in the many-body spectrum, there exists a manifold of states around 1 eV above the ground states with a redistribution of electrons within the d shell, which we attribute to the d-d excitations. An excess occupation in these excited states leads to a characteristic modification of the XAS signal, with a pronounced peak appearing below the main resonance (852 eV), a reduction of the spectral weight at the resonance (853 eV) and an additional increase around 854 eV. Even higher up in the spectrum, we identify a charge-transfer excitation [22,23], which results in a photoinduced peak roughly 0.5 eV lower in energy than the d-d peak. The latter also leads to a reduction of the spectral weight at the excitonic resonance.

For a more direct comparison with the experiment, we can combine the effects of screening and the photoinduced changes from the multiplet ligand field theory. Specifically, we consider a rigid band shift of $\omega_{\text{shift}} = 50$ meV of the XAS signal and add to it the photoinduced changes associated with two states with d-d and charge-transfer character, $\Delta\text{XAS}(\omega) = \text{XAS}(\omega)\text{-XAS}(\omega + \omega_{\text{shift}}) + \sum_{a=3,12} \Delta\text{XAS}[\omega, \rho[\alpha_a]]$ where $a = 3, 12$ refers to the states listed in Table I and the extra weights are set to $\alpha_a = 2\%$. We have checked that different choices for the nonthermal populations lead to qualitatively similar results. The comparison with the experiment shows an excellent agreement in the photo-renormalized XAS signal below and above the main excitonic resonance.

A comparison of photo- and chemical doping is instructive. Chemical doping leads to the appearance of a pre-edge feature at the O K edge [79] while such a pre-edge peak is absent at the Ni $L_{3,2}$ edges [80]. Photodoping produces the opposite result, i.e., the absence of a pre-edge feature at the O K edge (which by comparison to [79] would be expected at 527 eV), and the presence of such a feature at the Ni L_3 edge. The difference between chemically doped and photodoped spectra is a key observation, which shows that photodoped holes differ in nature from chemically dopes holes: They might

occupy different p-d hybrid orbitals (such as non-bonding configurations instead of the Zhang-Rice doublet [29]), or there may exist excitonic correlations between photodoped electrons and holes.

III. CONCLUSIONS

In conclusion, we showed that photodoping by above charge-transfer gap excitations in NiO results in characteristic transient signatures in XAS. These are (i) energy shifts of the excitonic peaks of several 10 meV for photodoping on the order of 1%, which persist for tens of ps due to the long lifetime of the photodoped state and are potentially enhanced by polaronic effects [64,67,77], and (ii) many-body multiplet excitations in the Ni L_3 pre-edge region. The good qualitative agreement between the tr-XAS measurements and a simple model for charge-transfer insulators suggests that energy shifts resulting from photoinduced changes in the electrostatic Hartree energy are a generic feature in transition metal oxides. Screening-induced changes in the interaction strengths play a role in determining these shifts. Theoretical comparison with high electron temperature calculations shows that the dominant effect on changes in screening is photodoping in contrast to electronic heating, but the detailed separation between the two would require longer simulation times. Our paper furthermore establishes that tr-XAS of photoexcited states is sensitive to the interaction between core electrons and ligand holes, which is important for a quantitative interpretation of the spectral changes. All these observations reveal generic signatures of charge-transfer insulators, providing a basis for future systematic analysis of these microscopic phenomena in this important material class, e.g., through the application of sum rules. Disentangling nonequilibrium multiplet effects from time-dependent renormalization of interaction parameters and Hartree shifts further promises to aid the design of tailored excitation protocols for reaching specific photodoped states.

APPENDIX A: SAMPLE PREPARATION AND CHARACTERIZATION

The NiO samples are grown using molecular beam epitaxy (MBE) on a 12×12 grid of 200-nm-thick Si_3N_4 membranes.
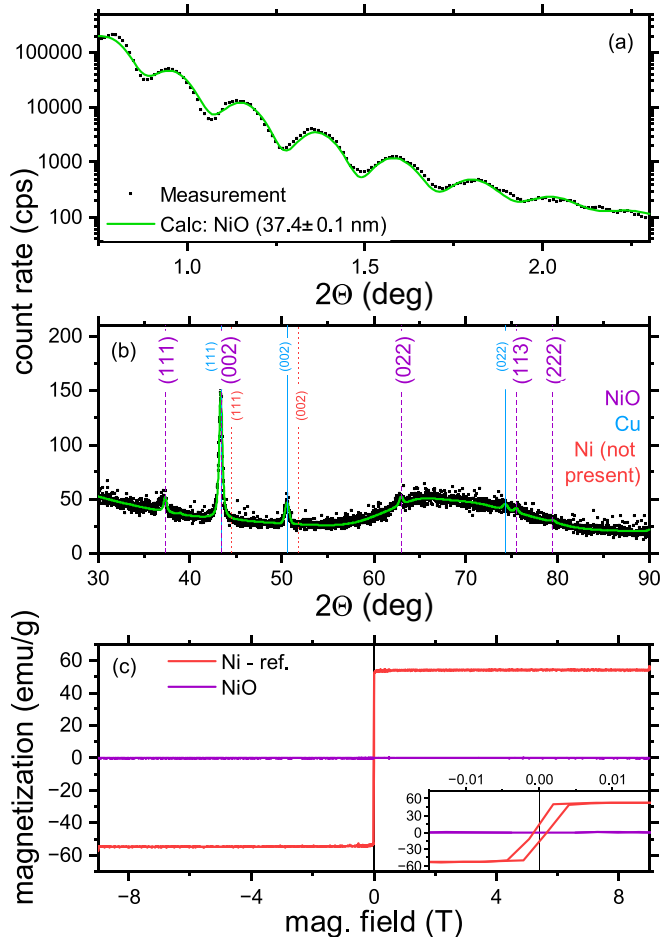
FIG. 6. (a) Small-angle x-ray diffraction pattern (black squares) and calculation (green line) for the determination of the NiO thickness as 37.4 ± 0.1 nm. (b) Wide-angle x-ray diffraction pattern (black squares), measured with a $5°$ offset to the Bragg condition, with a refined pattern (green line). The major peaks of NiO and Ni (for comparison) are highlighted with dashed purple lines and dotted red lines, respectively. The Cu peaks (blue lines) originate from the Cu heat sink on the back of the Si_3N_4 substrate. (c) Vibrating sample magnetometry data, measuring the magnetic moment as a function of the applied magnetic field for NiO (purple line) and a Ni reference sample (red line).

They are grown at room temperature in an oxygen atmosphere of 1×10^{-6} mbar (compared to 2×10^{-8} mbar base pressure) with a deposition rate of 0.005 Å/s. During the growth, a mask is used to cover specific rows of sample windows so that these bare Si_3N_4 windows can be used to measure a reference signal for the normalization of the intensity of the x-ray pulses. The thickness of the sample is monitored during the growth process using a quartz oscillator and later confirmed to be 37.4 ± 0.1 nm using small-angle x-ray diffraction. The sample characterization using x-ray diffraction and vibrating sample magnetometry is shown in Fig. 6. The x-ray diffraction pattern is measured with a $5°$ offset to the Bragg condition in order to suppress the (004) peak of Si, which comes from the grid underneath the Si_3N_4 membranes. In the x-ray diffraction pattern, we see the (111) and (002) peaks at $37.3°$ and $43.4°$ (highlighted by the dashed purple lines), indicating the

samples to be NiO. Furthermore, the absence of any peak around $44.5°$ and $51.8°$ (highlighted by the dotted red lines) shows that the sample is pure NiO and that there are no Ni contributions. The same can be seen in the magnetometry data comparing our samples to a Ni reference, where we find a vanishing magnetic moment for our NiO sample.

APPENDIX B: EXPERIMENTAL DETAILS AND DATA PROCESSING

This Appendix details additional experimental conditions and the steps taken in analyzing the experimental data. The absorption spectra are measured in transmission geometry in accordance with the employed beam-splitting off-axis zone plate setup [57] and are evaluated using the dedicated Spectroscopy and Coherent Scattering (SCS) Instrument toolbox [81]. For each measurement, 18 x-ray pulses of the free electron laser (FEL) bunch train were used with a temporal separation of 17.8 μs, which are synchronized with 16 laser pulses dropping the first and last x-ray pulse. From the transmitted signal, the x-ray absorption spectroscopy (XAS) is calculated as the negative logarithm of the transmitted signal divided by the reference signal, where the flat-field and non-linearity corrections [55] are also incorporated. Likewise, the pump-induced change is derived by taking the negative logarithm of the fraction between the excited spectrum and the ground-state spectrum. For the spectra displayed in the main manuscript, the first 9 pump/probe synchronized pulses of each train are used as the optimal compromise to enhance data quality while limiting the effects of lattice heating and long-lived excited states at high repetition rate.

1. Background correction

The evaluated Ni L_{23} edge absorption spectra show a background in the form of an offset between the ground state and excited spectrum, which we attribute to the zone plate setup. In addition, the two spectra slightly deviate over the measured energy range, as the offset increases slightly with increasing photon energy. The background is corrected using two identical linear functions of opposite signs, which are constructed from the difference between the spectra in the pre- and post-edge region. Thus the ground state and excited spectra coincide in the pre- and post-edge regions after the correction, as shown in Fig. 1(b). After the background correction, the spectra are normalized such that the mean value in the pre-edge corresponds to 0 while the mean value of the post-edge corresponds to 1, see Fig. 1(b). The induced changes, as determined by the SCS toolbox [81], are also corrected with the linear background function and then scaled according to the normalization of the spectra to ensure the agreement between the two. In order to also normalize the delay scans, an average normalization factor is determined from all the absorption spectra for each pump laser fluence, which is then used to scale the induced changes.

For the oxygen K edge, the background takes a more complicated form that cannot be captured with a linear approximation. The background still shows an offset like the Ni L_{23} edge spectra; however, the spectra appear to diverge with a quadratic background. From some of the delay scans that we measured, we can determine that in addition to the pre- and

post-edge regions, there are no pump-induced changes from 548 eV to 550 eV and from 563 eV to 565 eV. Using these regions as a reference, we can correct the background in the same manner as we did at the Ni L_{23} edges, using, however, a quadratic function rather than a linear one. Following the background correction, the spectra are also normalized such that the mean value in the pre-edge region corresponds to 0 while the mean value of the post-edge corresponds to 1.

2. Analysis of pump-induced changes

In order to analyze the experimental spectra, we extract the modifications of the ground-state spectrum that reproduce the excited-state spectrum. A rigid energy shift and a broadening are considered as individual modifications for the nickel L_{23} edges and oxygen K edge. We calculate an Akima spline of the ground-state spectrum and include the energy shift by shifting the energy axis by an amount ΔE relative to the original ground-state spectrum. The broadening is incorporated by convoluting this Akima spline with a Gaussian with the full width at half maximum (FWHM) ω. By calculating the difference between the Akima spline and ground-state spectrum, we get a modelled induced change that we can optimize with these two parameters. This modelled pump-induced change is optimized for the nickel L_{23} edges over the whole energy range (845–875 eV). For the oxygen K edge, we optimize the model at the measured induced changes of the first peak between 525 eV and 532.5 eV. This is done since using the whole energy range leads to an overall worse agreement of the model, because the second and fourth fine structure peaks show some additional modifications that are not described with an energy shift and broadening. By fixing one of the parameters to be zero, we can show that both modifications are necessary to describe the measured induced changes at the nickel L_{23} edges and oxygen K edge.

As the calculated spectra shown in Fig. 3(a) of the main text show a narrowing with increased photodoping, the model used to describe the pump-induced changes in the experimental data is not applicable to the calculations, in particular for larger photodoping values. Instead, in order to determine the energy shift and narrowing, a Voigt profile is fitted to the calculated data. The energy shift is then determined as the difference between the central peak positions, whereas the broadening/narrowing is determined as the difference between the overall FWHM. For smaller photodoping, the same modeling as for the experimental data as well as the fit of a Voigt profile can be applied, which show an overall excellent agreement for the determined energy shift. While the determined values for the broadening/narrowing deviate somewhat, the trends are still similar.

For the visual representation of the delay scans, an additional binning is applied. The initial binning of the delay scans is chosen such that a data point is measured every 80 fs to ensure that even the fastest response can be resolved. However, this time resolution is only necessary immediately before and following the laser excitation, as the induced change is long-lived. For an improved presentation, the scans are binned so that four data points are consolidated into one new data point at delays long after the laser excitation, as shown in Fig. 7. The line added in Fig. 7 and Fig. 2(a) of the main text
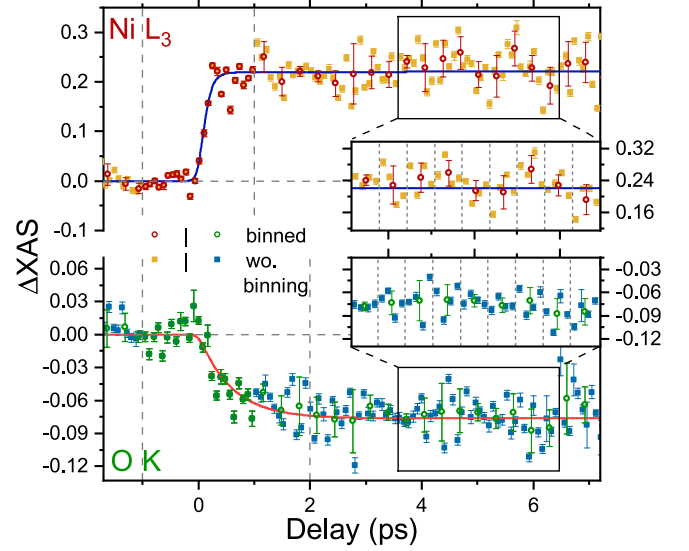
FIG. 7. Time-dependence of ΔXAS at the Ni L_3 (top) and O K (bottom) edge, for the excited charge carrier density of $dn = 4.7\%$ and different binning at longer delays.

is a guide for the eye and is obtained by fitting a response function [82],

$$A_0 + \Theta(t - t_0)\Big(A_1 \cdot \Big[1 - e^{\frac{-(t-t_0)}{\tau_1}}\Big] \cdot \Big[e^{\frac{-(t-t_0)}{\tau_2}}\Big]$$
$$+ A_2 \cdot \Big[1 - e^{\frac{-(t-t_0)}{\tau_2}}\Big]\Big). \tag{B1}$$

This function is convoluted with a Gaussian function with the FHWM $\Gamma_{tr} = 80$ fs to take into account the time resolution. For the shown delay scans, the second time constant τ_2 converges towards infinity if left unconstrained, as no recovery is apparent. As such, this time constant was fixed for the final fit to reduce the number of free parameters and increase the fit quality. The data is fitted to the original data and shows that there are no deviations resulting from the additional binning. The shown error bars are the standard deviation of the data points within one bin.

3. Calculation of excitation density

During the experiment, we measured the laser fluence to be 0.8 mJ/cm^2 and 4.0 mJ/cm^2 corresponding to the number of incoming photons (n_{ph}^{in}) of 1.07×10^{15} photons/cm^2 and 5.36×10^{15} photons/cm^2, respectively. In order to calculate the photoexcitation for comparison with theory, we first calculate the number of absorbed photons (n_{ph}^{abs}) using Beer-Lambert's law,

$$n_{ph}^{abs} = n_{ph}^{in} - n_{ph}^{in} \cdot e^{-\mu(E) \cdot d}. \tag{B2}$$

Here $\mu(E)$ is the absorption coefficient, which is set to 503000 1/cm according to Ref. [10], while d is the film thickness in cm. From this, we calculate the excitation density as $\frac{p_{e-} \cdot n_{ph}^{abs}}{d}$ e$^-$/cm^3, with p_{e-} being the probability of a photoexcitation, which we assume to be 0.55 as the average of the possible values between 0.1 and 1. This value is then normalized to the unit cell value of NiO, where we assume

the lattice constant to be 4.2 Å, resulting in the photodoping values dn of 0.9% (0.8 mJ/cm^2) and 4.7% (4.0 mJ/cm^2) with an estimated error of 82%.

APPENDIX C: EFFECTS OF LONG-LIVED EXCITED STATES AND DISTINCTION FROM X-RAY/LASER-INDUCED DAMAGE

In this Appendix, we discuss possible x-ray or laser-induced damage as well as the influence of extremely long-lived excited states on the measurements.

For our measurements, we can exclude any irreversible x-ray irradiation-related effects. We have two possible ways to test for x-ray irradiation damage effects. The European XFEL's bunch-train delivery pattern allows us to track changes in the unpumped spectra over the course of each train. Here, we do not observe any changes. Additionally, by comparing the spectral shape of subsequent unpumped spectra measured at the same sample position, we can further exclude any irreversible x-ray-related irradiation damage. By comparison with the results of [83], which were acquired with the same experimental setup, we can conclude that the FEL pulse energy in our experiments is orders of magnitude lower than the damage threshold, and as such, our samples incur no irreversible x-ray irradiation damage.

We observed irreversible laser irradiation damage only once during the early stages of the experiment, showing up as a strongly asymmetric signal on the DSSC detector [58], likely due to accidentally setting the pump fluence above the damage threshold. Additionally, in that case, we find a strong modification of the spectrum corresponding to the previously pumped sample window, even for a subsequent measurement without pump laser, i.e., irreversible changes. This is shown in Fig. 8. This data and the damaged sample were discarded in the further analysis; we confirmed that all other acquired datasets did not exhibit any such indication of sample damage.

However, one effect that we observe in our data that we were unable to circumvent during the experiments is the progressively increasing modification of the pumped XAS over the FEL train. This effect occurs even with the relatively large temporal spacing of 17.8 μs between each pump/probe synchronized pulse, which corresponds to an intratrain repetition rate of 56 kHz and is still visible within the unpumped 18th x-ray pulse of each FEL train. We can analyze this effect by investigating how the ΔXAS changes for an increased number of pump/probe synchronized pulses in each FEL train. We find that ΔXAS slightly increases with an increasing number of pulses for both the Ni $L_{2,3}$ and the O K edge, as shown in panel (a) of Figs. 9 and 10. The shape of this long-living contribution appears derivative-like and can be described by an increased energy shift and broadening, as demonstrated by the modeling included in the panel. Some features are, however, not affected, like the pre-edge feature at the Ni L_3 edge. Additionally, the contribution is independent of the set pump/probe time delay, as well as the laser fluence. To further analyze how this affects the spectral shape, we used our modeling approach to extract the values for the energy shift and broadening for an increasing number of bunches per train, which is shown in panel (b) of Figs. 9 and 10 for one exemplary scan with a pump/probe time delay of
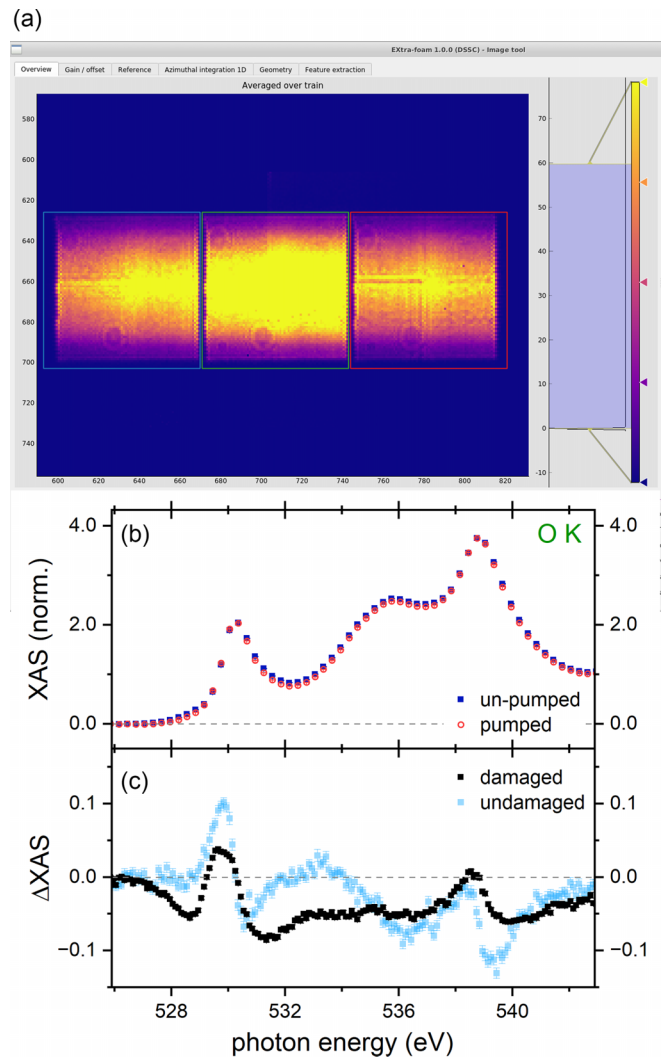
FIG. 8. (a) DSSC image averaged over a train with the three detector regions of interest marked corresponding to the pumped (left), reference (middle) and ground-state (right) signal. The strongly asymmetric intensities between the left and right regions of interest indicate sample damage. (b) Static measurement of the sample in (a) with the spectra corresponding to the ground-state (blue squares) and pumped (red circles) signals. (c) ΔXAS of the damaged (black) compared to an undamaged sample (light blue) at $\Delta t = 0.5$ ps.

0.5 ps and a laser fluence of 4 mJ/cm^2 for the Ni L_{23} and the O K-edge, respectively. The results of this analysis are reflected by the error bars of Fig. 2(b). Likely reasons for this effect are the occurrence of lattice heating and/or extremely long-lived excited states that have not fully decayed before the next pump/probe synchronized pulse arrives in the FEL train. Such long-lived states have previously been observed to occur in oxides [84]. Specifically, it has been shown that polaron trapping can occur in NiO [67]. A long-lived polaron state might also explain the more pronounced effect on the O K edge, as it was shown previously in MgO that the O K edge is particularly sensitive to lattice excitation [32,63]. We would like to note, however, that although this effect influences the determined energy parameters from our modeling, it can be considered simply as an additional error as it influences
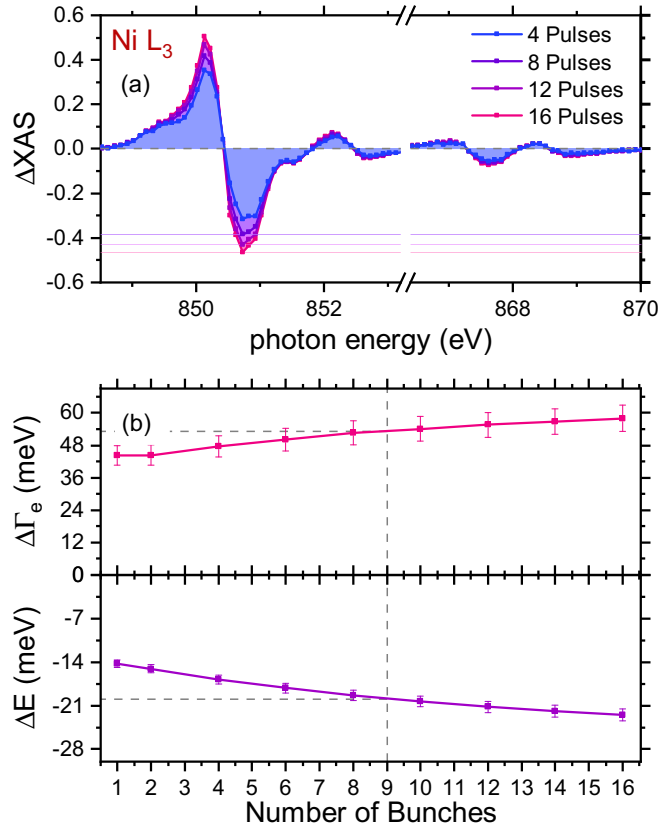
FIG. 9. (a) ΔXAS for the Ni $L_{2,3}$ edge with an increasing number of pulses in the bunch-train considered. (b) Values for the energy shift and broadening determined from the model by including an increasing number of bunches.

FIG. 10. (a) ΔXAS for the O K edge with an increasing number of pulses in the bunch-train considered. (b) Values for the energy shift and broadening determined from the model by including an increasing number of bunches.

neither the strength of the laser-induced dynamics nor the dynamics itself. Additionally, unless otherwise stated, for the data shown in the Appendix, we used a total of nine x-ray bunches, which limits the contribution of long-lived excited states to the observed spectral changes to about 20% at the Ni $L_{2,3}$ edges, which still allows the comparison to theory.

APPENDIX D: EVALUATION OF THE XAS SIGNAL IN (GW+)DMFT

Within DMFT-based simulations, the calculation of the XAS signal is handled in a postprocessing step (see Refs. [71,72] for a detailed description of the formalism in the time-resolved case). We start from the DMFT impurity model, which describes one d orbital embedded in the lattice. (For GW+EDMFT simulations, the impurity model includes both the fermionic environment, and the dynamically screened local interactions [70].) To this model we explicitly add the core level, so that the impurity Hamiltonian is extended by the terms

$$H_{\text{post}} = H_c + H_{\text{dip}} + H_{cd} + H_{cp}.$$

Here the first term H_c describes a single-core level,

$$H_c = \epsilon_c n_c,$$

where ϵ_c is the core level energy, n_c is the density operator for the core hole, and H_{dip} describes the dipolar transitions

between the core and valence orbitals. Because the x-ray energies ω_{in} (of the order of 1 keV) are much larger than the energies in the valence band (of the order of 1 eV), we treat the dipolar transitions from the core level to the d orbital within the rotating wave approximation, as detailed in Refs. [71,72]. In this case, the x-ray transition energies are determined relative to a given reference, which can be the core level energy $|\epsilon_c|$, or a constant shift thereof. Throughout this paper we choose the energy reference as the position of the main excitonic line in the unperturbed system, denoted by $|E_c|$. A core-hole typically decays within a few femtoseconds, mainly due to Auger processes [7]. This decay implies an extrinsic broadening of the XAS transition lines, in addition to intrinsic line-shape effects that are related to the valence band final states. In the DMFT formalism for time-resolved XAS [71], a near-exponential decay of the core hole is implemented by coupling the core level to an electron reservoir with a wide Gaussian density of states. We use a bandwidth $W/t_{dp} = 40.0$ for the bath, and choose the coupling strength to fix a lifetime $\Gamma = 0.05 \text{ fs}^{-1}$.

The interaction between a core hole and the valence electrons on the d site is described by a local density-density interaction with strength U_{cd} given by $H_{cd} = U_{cd}(n_c - 2)n_d$, where the shift of the core density is chosen such that the term vanishes for systems without core hole. The value of the core-valence interaction is comparable to the Coulomb

repulsion on the d orbital [12] and we have chosen them to be equal, $U_{cd} = 7.5$ eV $= U_{dd}$. We have checked that the photoinduced changes are robust with respect to variations of the core-valence interaction U_{cd}, up to a rigid shift of the XAS peaks. Similarly, we include the interaction between the core hole and the valence electrons on the p orbitals. We assume an interaction term $H_{cp} = U_{cp}(n_c - 2)N_p$, where N_p measures the total occupation on the four p orbitals adjacent to the probe site, analogous to the interaction U_{pd} in Hamiltonian (1). Within the DMFT framework, this non-local interaction enters the impurity model as a Hartree shift of the c orbital, $H_{cp}^{HF} = U_{cp}(n_c - 2)\langle N_p(t)\rangle$, where $\langle N_p(t)\rangle = 2\langle n_{p_x} + n_{p_y}\rangle$ is the occupation of the p orbitals obtained from the self-consistent GW+EDMFT simulation. (The factor two accounts for the fact that each correlated site has two neighboring p_x and two p_y orbitals; by symmetry, $\langle n_{p_x}\rangle = \langle n_{p_y}\rangle$).

APPENDIX E: TWO-BAND HUBBARD MODEL

The dynamics of the active e_g orbitals in NiO can be approximately described by the two-orbital Hubbard Hamiltonian

$$H = -t_{hop} \sum_{i,\alpha \in \{1,2\}} (c_{i\alpha}^\dagger c_{i\alpha} - \mu) + \sum_{i,\alpha} U n_{i\alpha\uparrow} n_{i\alpha\downarrow}$$
$$+ \sum_{i,\sigma} [(U - 2J_H)n_{i1\sigma}n_{i2\bar{\sigma}} + (U - 3J_H)n_{i1\sigma}n_{i2\sigma}], \quad (E1)$$

where i (α) is the site (orbital) index, t_{hop} is the hopping integral, U is the Coulomb repulsion and J_H is the Hund interaction.

We solve this model in the atomic limit and using DMFT on the Bethe lattice with bandwidth $W = 4$ eV, see also the analysis in Ref. [71]. In contrast to GW+EDMFT, the DMFT calculation cannot capture any bandgap renormalization, but it can describe the photogeneration of local many-body multiplets, like Hund or d-d excitations.

In the atomic limit, we label the local many-body multiplets as N_d, where N refers to the occupation and d to the spin state, with $d = h$ for the high spin, $d = l$ for the low spin and $d = s$ for the intra-orbital singlet. The main XAS resonance in the two-orbital half-filled Hubbard model corresponds to the transition $2_h \rightarrow \underline{3_d}$, where the underline indicates the presence of a core hole, and its energy is given by $\omega = E(\underline{3_d}) - E(2_h) = (U + J_H)/2 - U_{cd} - \epsilon_c$. After the photoexcitation additional transitions can be activated:

(1) $2_l \rightarrow \underline{3_d}$, whose energy is given by $\omega = E(\underline{3_d}) - E(2_l) = (U - J_H)/2 - U_{cd} - \epsilon_c$. This state corresponds to the main side peak in Fig. 11(a). As the difference to the main excitonic resonance is the spin configuration and not the charge configuration, the energy separation between these states is independent of the core-valence interaction U_{cd}.

(2) $2_s \rightarrow \underline{3_d}$, whose energy is given by $\omega = E(\underline{3_d}) - E(2_s) = (U - 5J_H)/2 - U_{cd} - \epsilon_c$. The energy difference of this transition to the main excitonic peak is independent of the core-valence interaction U_{cd}.

(3) $1_d \rightarrow \underline{2_h}$, whose energy is given by $\omega = E(\underline{2_h}) - E(1_d) = -(U + J_H)/2 - \epsilon_c$. This state has a different charge configuration than the main excitonic resonance and the
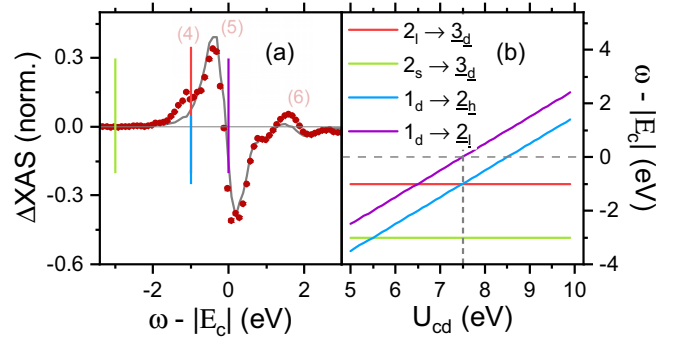
FIG. 11. (a) Experimental Ni L_3 ΔXAS at $\Delta t = 0.25$ ps and $dn = 0.86\%$ (points) with modeling as explained in the main text (grey line), and expected many-body multiplet transitions extracted from the atomic limit of a two-band Hubbard model (vertical lines). (b) Shifts of the relevant photoinduced transitions, relative to the main excitonic resonance $2_h \rightarrow \underline{3_d}$, with the core-valence interaction U_{cd}.

difference between the two will depend on the core-valence interaction U_{cd}, as presented in Fig. 11.

(4) $1_d \rightarrow \underline{2_l}$, whose energy is given by $\omega = E(\underline{2_l}) - E(1_d) = (-U + J_H)/2.0 - \epsilon_c$. The energy difference with respect to the main excitonic peak depends on the core-valence interaction U_{cd}.

(5) $\underline{3_d} \rightarrow \underline{4_d}$, whose energy is given by $\omega = E(\underline{4_d}) - E(\underline{3_d}) = \frac{3U - 5J_H}{2} - 2U_{cd} - \epsilon_c$. For parameters relevant for NiO this resonance appears deep below the main resonance.

The comparison between the atomic limit analysis and the experimental data is presented in Fig. 11(a) for $U_{cd} = U_{dd} = 7.5$ eV. In particular, the additional photoinduced resonances due to Hund excitations include $2_l \rightarrow \underline{3_d}$ and $2_s \rightarrow \underline{3_d}$ and they appear $J_H = 1$ eV or $3J_H = 3$ eV below the main excitonic peak [Fig. 11(a)] [28,49,51]. The experimental Ni L_3 ΔXAS pre-edge feature reasonably matches the energy of the transition $2_l \rightarrow \underline{3_d}$, see Fig. 11(a). There are no obvious signs of the $2_s \rightarrow \underline{3_d}$ transition at lower energy, as it presumably would only appear at even shorter Δt and/or higher pump frequencies and photodoping. For the core-valence interaction $U_{cd} = U_{dd} = 7.5$ eV, see Fig. 11(b), the $2_l \rightarrow \underline{3_d}$ Hund side peak is degenerate with the transition $1_d \rightarrow \underline{2_h}$. However, one would expect that holes on the Ni site will undergo a CT relaxation to the ligands on the femtosecond timescale, so that the 1_d-initial state would have a much shorter lifetime than the observed satellite.

A similar analysis can be performed for the oxygen K edge. The two relevant interactions are the Coulomb interaction between the nickel d orbital and oxygen p orbitals U_{dp} and the interaction between the core hole and the oxygen p orbitals U_{cp}. As these are density-density interactions, we only need to consider different charge configurations. We will use the notation (n_p, n_d, n_c) for the occupation on the p, d and core orbital, respectively. There are two relevant transitions:

(1) The resonance obtained from the ground state is given by $(6, 2, 2) \rightarrow (6, 3, 1)$ and its energy is given by $\omega = 6(U_{dp} - U_{cp}) - \epsilon_c$.

(2) $(5, 3, 2) \rightarrow (5, 4, 1)$ is the resonance relevant for the state after the charge-transfer excitation. Its energy is given by $\omega = 5(U_{dp} - U_{cp}) - \epsilon_c$.
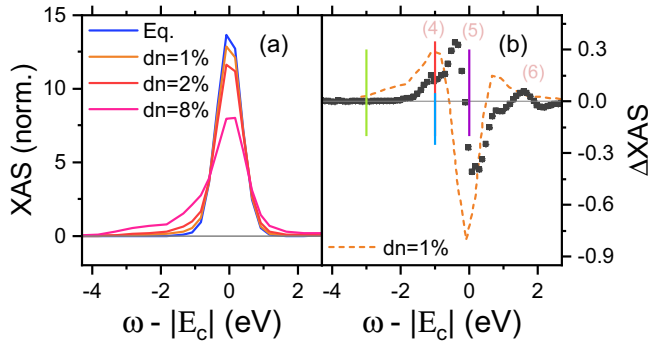
FIG. 12. (a) Calculated Ni L_3 XAS in equilibrium (blue line) and evaluated within the two-band Hubbard model for increasing dn as indicated. (b) Measured Ni L_3 ΔXAS at $\Delta t = 0.25$ ps (symbols) with vertical lines marking the positions of the atomic transitions (from left to right) $2_s \rightarrow \underline{3_d}$, $2_l \rightarrow \underline{3_d}$ (degenerate with $1_d \rightarrow \underline{2_h}$) and $2_h \rightarrow \underline{3_d}$ (degenerate with $1_d \rightarrow \underline{2_l}$). The dashed line corresponds to the model calculation with d$n = 1\%$. We have fixed the parameters of the model to $U = U_{cd} = 7.5$ eV, $J_H = 1$ eV, $\beta = 5$ eV^{-1}.

The above analysis shows that the oxygen shift is determined by a subtle balance between U_{dp} and U_{cp}. It is an important future task to determine these parameters from first principles in equilibrium, compute the equilibrium spectrum, and then analyze these shifts after a photoexcitation.

The atomic limit analysis is consistent with the full DMFT simulation of the photoexcited system, as shown in Fig. 12(a) for $dn = 1\%$ photodoping. Here, the system is excited by a hopping modulation pulse with an envelope $a_{\text{pump}} \exp[-(t - t_{\text{pump}})^4]$ centered at time $t_{\text{pump}} = 1.5$ eV^{-1} and with amplitude $a_{\text{pump}} = 0.15$ eV. (In equilibrium, the hopping parameter t_{hop}^* in the Bethe lattice calculation is related to the bandwidth by $W = 4t_{\text{hop}}^*$.) The XAS probe pulse has an envelope $a_{\text{probe}} \exp[-(t - t_{\text{probe}})^2/8]$ centered at $t_{\text{probe}} = 6.5$ eV^{-1} and amplitude $a_{\text{probe}} = 0.01$ eV. We use here a setup with explicit core level at energy -20 eV, as described in Ref [71].

These DMFT simulations show that the photoinduced transition with the highest weight is $2_l \rightarrow \underline{3_d}$, although there also appears a pronounced shoulder corresponding to the transition $2_s \rightarrow \underline{3_d}$ for higher photodopings. The DMFT and atomic limit analysis agree with the position of the experimental side peak, as shown in Fig. 12(b), but these calculations cannot capture the combined effect of the bandgap renormalization and the side peak appearance. Describing both effects would require an extension of the GW+EDMFT formalism to a two-orbital problem on the d site, which is an important future challenge. Our results, nevertheless, suggest that with future experimental advances in time-resolved XAS it may become possible to measure the occupations of local many-body states, since these are directly reflected in the heights of the photoinduced resonances.

In this analysis, we restricted our attention to the dynamics within the e_g orbitals and neglected the contributions from charge-transfer or d-d excitations. We relax this approximation in the next Appendix, where we consider a nonthermal extension of the multiplet ligand-field theory.

APPENDIX F: NONTHERMAL MULTIPLET LIGAND-FIELD THEORY

This Appendix describes the nonthermal multiplet ligand field theory used in the main text to estimate the nonthermal signatures from excited states in the XAS signal. The analysis is motivated by recent time-dependent DMFT simulations of XAS in multiorbital Hubbard models [71], which showed that after a photoexcitation, the atomic XAS spectrum computed with the nonthermal state populations provides a good approximation to the full nonequilibrium DMFT result. This allows us to combine the multiplet ligand field theory with a quasistationary approach, where we replace the Boltzmann distribution by a nonthermal distribution featuring an excess population of certain low-lying excited states. The calculations follow Ref. [16] and the implementation is based on the EDRIXS [78] library.

The theoretical description employs ligand orbitals, which are constructed as a linear superposition of the oxygen Wannier orbitals coupling to a given $3d$ orbital. These orbitals are used to construct a generalized Anderson impurity problem [16],

$$
\begin{aligned}
H = &\sum_{ij} \epsilon_{d,i} d_i^\dagger d_i + \sum_i \left(\epsilon_{b,i} b_i^\dagger b_i + \sum_j V_{ij} [d_j^\dagger b_i + \text{H.c.}] \right) \\
&+ \zeta_d \sum_{ij} \langle d_i | \vec{l}\vec{s} | d_j \rangle d_i^\dagger d_j + \sum_{ijkl} U_{ijkl}^d d_i^\dagger d_j^\dagger d_l d_k \\
&+ \sum_i \epsilon_p p_i^\dagger p_i + \zeta_p \sum_{ij} \langle p_i | \vec{l}\vec{s} | p_j \rangle p_i^\dagger p_j \\
&+ \sum_{ijkl} U_{ijkl}^{pd} d_i^\dagger p_j^\dagger p_l d_k,
\end{aligned}
\tag{F1}
$$

where the d_i, b_i, and p_i are the annihilation operators for electrons at site i on the d orbital, bath orbital and core p orbital, respectively. The corresponding single-particle energies without spin-orbit coupling are given by $\epsilon_{d,i}$, ϵ_b, and ϵ_p. The spin-orbit coupling on the d (p) orbital is described by ζ_d (ζ_p), the angular momentum operator $\vec{l}$ and the spin operator $\vec{s}$. The Coulomb repulsion between the $3d$ electrons is given by the rank-4 tensor U^d and the repulsion between the $3d$ and $2p$ orbitals by the tensor U^{pd}.

The spherical part of the interaction, parametrized by the Hubbard repulsion U, is strongly screened and is typically determined by a fit to experiments. In the following, we will use the parameters from Ref. [16], namely $U_{dd} = 7.3$ eV and $U_{pd} = 8.5$ eV. The rest of the interaction parameters are estimated by the atomic Hartree-Fock calculation and reduced to 80% of the bare value to account for screening. The atomic Coulomb interactions are typically parametrized by the Slater-Condon parameters. We use the screened values $F_{0,dd} = U_{dd} + \frac{2}{63}[F_{2,dd} + F_{4,dd}]$, $F_{2,dd} = 9.78$ eV, $F_{4,dd} = 6.07$ eV. Similarly, for the interaction between the valence d and the core p orbitals, we use $F_{0,pd} = U_{pd} + \frac{1}{15}G_{1,pd} + G_{3,pd}$, $G_{1,pd} = 4.63$ eV, $G_{3,pd} = 2.63$ eV.

In the cubic environment, the on-site energies on the impurity (bath) site take the values

$$
\epsilon_{d,i} = \epsilon_d + a_i 10\text{Dq}, \quad \epsilon_{b,i} = \epsilon_b + a_i \Delta_b,
$$

where 10Dq (Δ_b) is the crystal-field splitting between the e_g and t_{2g} orbitals on the impurity (bath) site and $a_{e_g} = 0.6$, $a_{t_{2g}} = -0.4$. To connect it with the on-site energies we need to solve the following linear set of equations [16,26,78],

$$10\epsilon_b + n\epsilon_d + \frac{n(n-1)}{2}U_{dd} = 0,$$

$$9\epsilon_b + (n+1)\epsilon_d + \frac{(n+1)n}{2}U_{dd} = \Delta,$$

$$8\epsilon_b + (n+2)\epsilon_d + \frac{(n+1)(n+2)}{2}U_{dd} = 2\Delta + U_{dd}, \quad \text{(F2)}$$

and a similar one for the system in the presence of the core hole. For the charge-transfer interaction, we use $\Delta = 4.7$ eV, for the crystal-field splitting on the impurity 10Dq $= 0.56$ eV and on the bath site $\Delta_b = 1.44$ eV. Finally, the spin-orbit coupling is obtained from the atomic values. For the core level, it is given by $\zeta_p = 11.5$ eV and for the valence orbital by $\zeta_d = 0.083$ eV (without core hole) or $\zeta_d = 0.102$ eV (with core hole). Finally, the hybridization amplitudes between the impurity and the bath are taken from Ref. [16]. In the e_g subspace it is given by $V_{e_g} = 2.06$ eV and in the t_{2g} subspace by $V_{t_{2g}} = 1.21$ eV.

[1] C. Giannetti, M. Capone, D. Fausti, M. Fabrizio, F. Parmigiani, and D. Mihailovic, Ultrafast optical spectroscopy of strongly correlated materials and high-temperature superconductors: A non-equilibrium approach, Adv. Phys. **65**, 58 (2016).

[2] A. de la Torre, D. M. Kennes, M. Claassen, S. Gerber, J. W. McIver, and M. A. Sentef, Colloquium: Nonthermal pathways to ultrafast control in quantum materials, Rev. Mod. Phys. **93**, 041002 (2021).

[3] Y. Murakami, D. Goleži, M. Eckstein, and P. Werner, Photo-induced nonequilibrium states in Mott insulators, arXiv:2310.05201.

[4] G. A. Sawatzky and J. W. Allen, Magnitude and origin of the band gap in NiO, Phys. Rev. Lett. **53**, 2339 (1984).

[5] J. Zaanen, G. A. Sawatzky, and J. W. Allen, Band gaps and electronic structure of transition-metal compounds, Phys. Rev. Lett. **55**, 418 (1985).

[6] J. Zaanen, C. Westra, and G. A. Sawatzky, Determination of the electronic structure of transition-metal compounds: $2p$ x-ray photoemission spectroscopy of the nickel dihalides, Phys. Rev. B **33**, 8060 (1986).

[7] F. M. de Groot, H. Elnaggar, F. Frati, R.-p. Wang, M. U. Delgado-Jaime, M. van Veenendaal, J. Fernandez-Rodriguez, M. W. Haverkort, R. J. Green, G. van der Laan *et al.*, $2p$ x-ray absorption spectroscopy of $3d$ transition metal systems, J. Electron Spectrosc. Relat. Phenom. **249**, 147061 (2021).

[8] L. J. P. Ament, M. van Veenendaal, T. P. Devereaux, J. P. Hill, and J. van den Brink, Resonant inelastic x-ray scattering studies of elementary excitations, Rev. Mod. Phys. **83**, 705 (2011).

[9] C. Y. Kuo, T. Haupricht, J. Weinen, H. Wu, K. D. Tsuei, M. Haverkort, A. Tanaka, and L. Tjeng, Challenges from experiment: Electronic structure of NiO, Eur. Phys. J.: Spec. Top. **226**, 2445 (2017).

[10] R. Newman and R. M. Chrenko, Optical properties of nickel oxide, Phys. Rev. **114**, 1507 (1959).

[11] R. Powell and W. Spicer, Optical properties of NiO and CoO, Phys. Rev. B **2**, 2182 (1970).

[12] G. van der Laan, J. Zaanen, G. A. Sawatzky, R. Karnatak, and J.-M. Esteva, Comparison of x-ray absorption with x-ray photoemission of nickel dihalides and NiO, Phys. Rev. B **33**, 4253 (1986).

[13] G. van der Laan, B. T. Thole, G. A. Sawatzky, and M. Verdaguer, Multiplet structure in the $L_{2,3}$ x-ray-absorption spectra: A fingerprint for high- and low-spin Ni^{2+} compounds, Phys. Rev. B **37**, 6587(R) (1988).

[14] F. de Groot, X-ray absorption of transition metal oxides: An overview of the theoretical approaches, J. Electron Spectrosc. Relat. Phenom. **62**, 111 (1993).

[15] A. Tanaka and T. Jo, Resonant $3d$, $3p$ and $3s$ photoemission in transition metal oxides predicted at $2p$ threshold, J. Phys. Soc. Jpn. **63**, 2788 (1994).

[16] M. W. Haverkort, M. Zwierzycki, and O. K. Andersen, Multiplet ligand-field theory using Wannier orbitals, Phys. Rev. B **85**, 165113 (2012).

[17] O. Šipr, J. Minár, A. Scherz, H. Wende, and H. Ebert, Many-body effects in x-ray absorption and magnetic circular dichroism spectra within the LSDA+DMFT framework, Phys. Rev. B **84**, 115102 (2011).

[18] M. Haverkort, G. Sangiovanni, P. Hansmann, A. Toschi, Y. Lu, and S. Macke, Bands, resonances, edge singularities and excitons in core level spectroscopy investigated within the dynamical mean-field theory, Europhys. Lett. **108**, 57004 (2014).

[19] P. S. Cornaglia and A. Georges, Theory of core-level photoemission and the x-ray edge singularity across the Mott transition, Phys. Rev. B **75**, 115112 (2007).

[20] A. Hariki, T. Uozumi, and J. Kuneš, LDA+DMFT approach to core-level spectroscopy: Application to $3d$ transition metal compounds, Phys. Rev. B **96**, 045111 (2017).

[21] K. Okada and A. Kotani, Intersite Coulomb interactions in quasi-one-dimensional copper oxides, J. Phys. Soc. Jpn. **66**, 341 (1997).

[22] S. Agrestini, K. Chen, C.-Y. Kuo, L. Zhao, H.-J. Lin, C.-T. Chen, A. Rogalev, P. Ohresser, T.-S. Chan, S.-C. Weng, G. Auffermann, A. Völzke, A. C. Komarek, K. Yamaura, M. W. Haverkort, Z. Hu, and L. H. Tjeng, Nature of the magnetism of iridium in the double perovskite $Sr_2 CoIrO_6$, Phys. Rev. B **100**, 014443 (2019).

[23] T. Burnus, Z. Hu, H. H. Hsieh, V. L. J. Joly, P. A. Joy, M. W. Haverkort, H. Wu, A. Tanaka, H.-J. Lin, C. T. Chen, and L. H. Tjeng, Local electronic structure and magnetic properties of $LaMn_{0.5}Co_{0.5}O_3$ studied by x-ray absorption and magnetic circular dichroism spectroscopy, Phys. Rev. B **77**, 125124 (2008).

[24] M. Rossi, H. Lu, A. Nag, D. Li, M. Osada, K. Lee, B. Y. Wang, S. Agrestini, M. Garcia-Fernandez, J. J. Kas, Y.-D. Chuang, Z. X. Shen, H. Y. Hwang, B. Moritz, K.-J. Zhou, T. P. Devereaux, and W. S. Lee, Orbital and spin character of doped carriers in infinite-layer nickelates, Phys. Rev. B **104**, L220505 (2021).

[25] T. M. Schuler, D. L. Ederer, S. Itza-Ortiz, G. T. Woods, T. A. Callcott, and J. C. Woicik, Character of the insulating state in NiO: A mixture of charge-transfer and Mott-Hubbard character, Phys. Rev. B **71**, 115113 (2005).

[26] J. Lüder, J. Schött, B. Brena, M. W. Haverkort, P. Thunström, O. Eriksson, B. Sanyal, I. Di Marco, and Y. O. Kvashnin, Theory of L-edge spectroscopy of strongly correlated systems, Phys. Rev. B **96**, 245131 (2017).

[27] M. Taguchi, M. Matsunami, Y. Ishida, R. Eguchi, A. Chainani, Y. Takata, M. Yabashi, K. Tamasaku, Y. Nishino, T. Ishikawa, Y. Senba, H. Ohashi, and S. Shin, Revisiting the valence-band and core-level photoemission spectra of NiO, Phys. Rev. Lett. **100**, 206401 (2008).

[28] J. Kuneš, V. I. Anisimov, A. V. Lukoyanov, and D. Vollhardt, Local correlations and hole doping in NiO: A dynamical mean-field study, Phys. Rev. B **75**, 165115 (2007).

[29] J. Bała, A. M. Oleś, and J. Zaanen, Zhang-rice localization, quasiparticle dispersions, and the photoemission of NiO, Phys. Rev. Lett. **72**, 2600 (1994).

[30] C. Stamm, N. Pontius, T. Kachel, M. Wietstruk, and H. A. Dürr, Femtosecond x-ray absorption spectroscopy of spin and orbital angular momentum in photoexcited Ni films during ultrafast demagnetization, Phys. Rev. B **81**, 104425 (2010).

[31] A. D. Smith, T. Balčiunas, Y.-P. Chang, C. Schmidt, K. Zinchenko, F. B. Nunes, E. Rossi, V. Svoboda, Z. Yin, J.-P. Wolf, and H. J. Wörner, Femtosecond soft-x-ray absorption spectroscopy of liquids with a water-window high-harmonic source, J. Phys. Chem. Lett. **11**, 1981 (2020).

[32] N. Rothenbach, M. E. Gruner, K. Ollefs, C. Schmitz-Antoniak, S. Salamon, P. Zhou, R. Li, M. Mo, S. Park, X. Shen, S. Weathersby, J. Yang, X. J. Wang, R. Pentcheva, H. Wende, U. Bovensiepen, K. Sokolowski-Tinten, and A. Eschenlohr, Microscopic nonequilibrium energy transfer dynamics in a photoexcited metal/insulator heterostructure, Phys. Rev. B **100**, 174301 (2019).

[33] E. Diesen, H.-Y. Wang, S. Schreck, M. Weston, H. Ogasawara, J. LaRue, F. Perakis, M. Dell'Angela, F. Capotondi, L. Giannessi, E. Pedersoli, D. Naumenko, I. Nikolov, L. Raimondi, C. Spezzani, M. Beye, F. Cavalca, B. Liu, J. Gladh, S. Koroidov *et al.*, Ultrafast adsorbate excitation probed with subpicosecond-resolution x-ray absorption spectroscopy, Phys. Rev. Lett. **127**, 016802 (2021).

[34] T. P. H. Sidiropoulos, N. Di Palo, D. E. Rivas, S. Severino, M. Reduzzi, B. Nandy, B. Bauerhenne, S. Krylow, T. Vasileiadis, T. Danz, P. Elliott, S. Sharma, K. Dewhurst, C. Ropers, Y. Joly, M. E. Garcia, M. Wolf, R. Ernstorfer, and J. Biegert, Probing the energy conversion pathways between light, carriers, and lattice in real time with attosecond core-level spectroscopy, Phys. Rev. X **11**, 041060 (2021).

[35] T. Lojewski, M. F. Elhanoty, L. L. Guyader, O. Grånäs, N. Agarwal, C. Boeglin, R. Carley, A. Castoldi, C. David, C. Deiter *et al.*, The interplay of local electron correlations and ultrafast spin dynamics in fcc Ni, Mater. Res. Lett. **11**, 655 (2023).

[36] D. R. Baykusheva, H. Jang, A. A. Husain, S. Lee, S. F. R. TenHuisen, P. Zhou, S. Park, H. Kim, J.-K. Kim, H.-D. Kim, M. Kim, S.-Y. Park, P. Abbamonte, B. J. Kim, G. D. Gu, Y. Wang, and M. Mitrano, Ultrafast renormalization of the on-site Coulomb repulsion in a cuprate superconductor, Phys. Rev. X **12**, 011013 (2022).

[37] X. Wang, R. Y. Engel, I. Vaskivskyi, D. Turenne, V. Shokeen, A. Yaroslavtsev, O. Grånäs, R. Knut, J. O. Schunck, S. Dziarzhytski *et al.*, Ultrafast manipulation of the NiO antiferromagnetic order via sub-gap optical excitation, Faraday Discuss. **237**, 300 (2022).

[38] O. Grånäs, I. Vaskivskyi, X. Wang, P. Thunström, S. Ghimire, R. Knut, J. Söderström, L. Kjellsson, D. Turenne, R. Y. Engel, M. Beye, J. Lu, D. J. Higley, A. H. Reid, W. Schlotter, G. Coslovich, M. Hoffmann, G. Kolesov, C. Schüßler-Langeheine, A. Styervoyedov *et al.*, Ultrafast modification of the electronic structure of a correlated insulator, Phys. Rev. Res. **4**, L032030 (2022).

[39] N. Tancogne-Dejean, M. A. Sentef, and A. Rubio, Ultrafast transient absorption spectroscopy of the charge-transfer insulator NiO: Beyond the dynamical Franz-Keldysh effect, Phys. Rev. B **102**, 115106 (2020).

[40] L. Stojchevska, I. Vaskivskyi, T. Mertelj, P. Kusar, D. Svetin, S. Brazovskii, and D. Mihailovic, Ultrafast switching to a stable hidden quantum state in an electronic crystal, Science **344**, 177 (2014).

[41] J. Li, H. U. R. Strand, P. Werner, and M. Eckstein, Theory of photoinduced ultrafast switching to a spin-orbital ordered hidden phase, Nat. Commun. **9**, 4581 (2018).

[42] T. Kaneko, T. Shirakawa, S. Sorella, and S. Yunoki, Photoinduced η pairing in the Hubbard model, Phys. Rev. Lett. **122**, 077002 (2019).

[43] J. Li, D. Golez, P. Werner, and M. Eckstein, Superconducting optical response of photodoped Mott insulators, Mod. Phys. Lett. B **34**, 2040054 (2020).

[44] D. Golež, L. Boehnke, M. Eckstein, and P. Werner, Dynamics of photodoped charge transfer insulators, Phys. Rev. B **100**, 041111(R) (2019).

[45] N. Tancogne-Dejean, M. A. Sentef, and A. Rubio, Ultrafast modification of Hubbard U in a strongly correlated material: *Ab initio* high-harmonic generation in NiO, Phys. Rev. Lett. **121**, 097402 (2018).

[46] M. Sandri and M. Fabrizio, Nonequilibrium gap collapse near a first-order Mott transition, Phys. Rev. B **91**, 115102 (2015).

[47] Z. He and A. J. Millis, Photoinduced phase transitions in narrow-gap Mott insulators: The case of VO$_2$, Phys. Rev. B **93**, 115126 (2016).

[48] S. Beaulieu, S. Dong, N. Tancogne-Dejean, M. Dendzik, T. Pincelli, J. Maklar, R. P. Xian, M. A. Sentef, M. Wolf, A. Rubio *et al.*, Ultrafast dynamical Lifshitz transition, Sci. Adv. **7**, eabd9275 (2021).

[49] H. U. R. Strand, D. Golež, M. Eckstein, and P. Werner, Hund's coupling driven photocarrier relaxation in the two-band Mott insulator, Phys. Rev. B **96**, 165104 (2017).

[50] J. Rincón, E. Dagotto, and A. E. Feiguin, Photoinduced Hund excitons in the breakdown of a two-orbital Mott insulator, Phys. Rev. B **97**, 235104 (2018).

[51] K. Gillmeister, D. Golez, C.-T. Chiang, N. Bittner, Y. Pavlyukh, J. Berakdar, P. Werner, and W. Widdra, Ultrafast coupled charge and spin dynamics in strongly correlated NiO, Nat. Commun. **11**, 4095 (2020).

[52] A. Müller, F. Grandi, and M. Eckstein, Ultrafast control of spin-orbital separation probed with time-resolved resonant inelastic x-ray scattering, Phys. Rev. B **106**, L121107 (2022).

[53] A. Georges, G. Kotliar, W. Krauth, and M. J. Rozenberg, Dynamical mean-field theory of strongly correlated fermion

systems and the limit of infinite dimensions, Rev. Mod. Phys. **68**, 13 (1996).

[54] H. Aoki, N. Tsuji, M. Eckstein, M. Kollar, T. Oka, and P. Werner, Nonequilibrium dynamical mean-field theory and its applications, Rev. Mod. Phys. **86**, 779 (2014).

[55] L. Le Guyader, A. Eschenlohr, M. Beye, W. Schlotter, F. Döring, C. Carinan, D. Hickin, N. Agarwal, C. Boeglin, U. Bovensiepen *et al.*, Photon-shot-noise-limited transient absorption soft x-ray spectroscopy at the European XFEL, J. Synchrotron Radiat. **30**, 284 (2023).

[56] Data recorded for the experiment at the European XFEL under proposal number 2589, doi:10.22003/xfel.eu-data-002589-00.

[57] F. Döring, B. Rösner, M. Langer, A. Kubec, A. Kleibert, J. Raabe, C. A. F. Vaz, M. Lebugle, and C. David, Multifocus off-axis zone plates for x-ray free-electron laser experiments, Optica **7**, 1007 (2020).

[58] M. Porro *et al.*, The MiniSDD-Based 1-Mpixel Camera of the DSSC Project for the European XFEL, IEEE Trans. Nucl. Sci. **68**, 1334 (2021).

[59] R. Sensarma, D. Pekker, E. Altman, E. Demler, N. Strohmaier, D. Greif, R. Jördens, L. Tarruell, H. Moritz, and T. Esslinger, Lifetime of double occupancies in the Fermi-Hubbard model, Phys. Rev. B **82**, 224302 (2010).

[60] Z. Lenarčič and P. Prelovšek, Ultrafast charge recombination in a photoexcited Mott-Hubbard insulator, Phys. Rev. Lett. **111**, 016401 (2013).

[61] D. Golež, L. Boehnke, H. U. R. Strand, M. Eckstein, and P. Werner, Nonequilibrium GW+EDMFT: Antiscreening and inverted populations from nonlocal correlations, Phys. Rev. Lett. **118**, 246402 (2017).

[62] D. Golež, M. Eckstein, and P. Werner, Dynamics of screening in photodoped Mott insulators, Phys. Rev. B **92**, 195123 (2015).

[63] N. Rothenbach, M. E. Gruner, K. Ollefs, C. Schmitz-Antoniak, S. Salamon, P. Zhou, R. Li, M. Mo, S. Park, X. Shen, S. Weathersby, J. Yang, X. J. Wang, O. Sipr, H. Ebert, K. Sokolowski-Tinten, R. Pentcheva, U. Bovensiepen, A. Eschenlohr, and H. Wende, Effect of lattice excitations on transient near-edge x-ray absorption spectroscopy, Phys. Rev. B **104**, 144302 (2021).

[64] R. Karsthof, M. Grundmann, A. M. Anton, and F. Kremer, Polaronic interacceptor hopping transport in intrinsically doped nickel oxide, Phys. Rev. B **99**, 235201 (2019).

[65] D. Ishikawa, M. W. Haverkort, and A. Q. Baron, Lattice and magnetic effects on a d–d excitation in NiO using a 25 meV resolution x-ray spectrometer, J. Phys. Soc. Jpn. **86**, 093706 (2017).

[66] F. G. Santomauro, J. Grilj, L. Mewes, G. Nedelcu, S. Yakunin, T. Rossi, G. Capano, A. Al Haddad, J. Budarz, D. Kinschel *et al.*, Localized holes and delocalized electrons in photoexcited inorganic perovskites: Watching each atomic actor by picosecond X-ray absorption spectroscopy, Struct. Dyn. **4**, 044002 (2017).

[67] S. Biswas, J. Husek, S. Londo, and L. R. Baker, Ultrafast electron trapping and defect-mediated recombination in NiO probed by femtosecond extreme ultraviolet reflection-absorption spectroscopy, J. Phys. Chem. Lett. **9**, 5047 (2018).

[68] J. Yu, K. M. Rosso, and S. M. Bruemmer, Charge and ion transport in NiO and aspects of Ni oxidation from first principles, J. Phys. Chem. C **116**, 1948 (2012).

[69] V. Emery, Theory of high-T_c superconductivity in oxides, Phys. Rev. Lett. **58**, 2794 (1987).

[70] D. Golež, M. Eckstein, and P. Werner, Multiband nonequilibrium GW+EDMFT formalism for correlated insulators, Phys. Rev. B **100**, 235117 (2019).

[71] P. Werner, D. Golez, and M. Eckstein, Local interpretation of time-resolved x-ray absorption in Mott insulators: Insights from nonequilibrium dynamical mean-field theory, Phys. Rev. B **106**, 165106 (2022).

[72] D. Golez, E. Paprotzki, P. Werner, and M. Eckstein, Measuring the ultrafast screening of U in photo-excited charge-transfer insulators with time-resolved X-ray absorption spectroscopy, arXiv:2409.06314.

[73] N. Dasari, J. Li, P. Werner, and M. Eckstein, Photoinduced strange metal with electron and hole quasiparticles, Phys. Rev. B **103**, L201116 (2021).

[74] P. Werner and M. Eckstein, Field-induced polaron formation in the Holstein-Hubbard model, Europhys. Lett. **109**, 37002 (2015).

[75] P. Erhart, A. Klein, D. Åberg, and B. Sadigh, Efficacy of the DFT+U formalism for modeling hole polarons in perovskite oxides, Phys. Rev. B **90**, 035204 (2014).

[76] F. Aryasetiawan, M. Imada, A. Georges, G. Kotliar, S. Biermann, and A. I. Lichtenstein, Frequency-dependent local interactions and low-energy effective models from electronic structure calculations, Phys. Rev. B **70**, 195104 (2004).

[77] L. M. Carneiro, S. K. Cushing, C. Liu, Y. Su, P. Yang, A. P. Alivisatos, and S. R. Leone, Excitation-wavelength-dependent small polaron trapping of photoexcited carriers in α-Fe_2O_3, Nat. Mater. **16**, 819 (2017).

[78] Y. Wang, G. Fabbris, M. Dean, and G. Kotliar, EDRIXS: An open source toolkit for simulating spectra of resonant inelastic x-ray scattering, Comput. Phys. Commun. **243**, 151 (2019).

[79] P. Kuiper, G. Kruizinga, J. Ghijsen, G. A. Sawatzky, and H. Verweij, Character of holes in $Li_xNi_{1-x}O$ and their magnetic behavior, Phys. Rev. Lett. **62**, 221 (1989).

[80] J. van Elp, B. Searle, G. Sawatzky, and M. Sacchi, Ligand hole induced symmetry mixing of d^8 states in $Li_xNi_{1-x}O$, as observed in Ni $2p$ x-ray absorption spectroscopy, Solid State Commun. **80**, 67 (1991).

[81] L. LeGuyader, SCS toolbox (2022), git.xfel.eu/SCS/ToolBox.

[82] N. Del Fatti, C. Voisin, M. Achermann, S. Tzortzakis, D. Christofilos, and F. Vallée, Nonequilibrium electron dynamics in noble metals, Phys. Rev. B **61**, 16956 (2000).

[83] R. Y. Engel, O. Alexander, K. Atak, U. Bovensiepen, J. Buck, R. Carley, M. Cascella, V. Chardonnet, G. S. Chiuzbaian, C. David *et al.*, Electron population dynamics in resonant non-linear x-ray absorption in nickel at a free-electron laser, Struct. Dyn. **10**, 054501 (2023).

[84] L. Foglia, S. Vempati, B. Tanda Bonkano, L. Gierster, M. Wolf, S. Sadofev, and J. Stähler, Revealing the competing contributions of charge carriers, excitons, and defects to the non-equilibrium optical properties of ZnO, Struct. Dyn. **6**, 034501 (2019).